Materials Transactions, Vol. 47, No. 8 (2006) pp. 1985 to 1993

Strengthening and Toughness of AZ61 Mg with Nano SiO_2 Particles

Y. P. Hung[1], J. C. Huang[1,*], K. J. Wu[2] and Chi Y. A. Tsao[2]

[1]*Inst. Materials Science and Engineering; Center for Nanoscience and Nanotechnology, National Sun Yat-Sen University, Kaohsiung, Taiwan 804, Republic of China*
[2]*Department of Materials Science and Engineering, National Cheng Kung University, Tainan 700, Taiwan, Republic of China*

The strengthening mechanisms and bending toughness of the AZ61 Mg based composites reinforced by nano SiO_2 particles are examined. The composites were prepared either by spray forming, ingot metallurgy, or powder metallurgy, followed by severe hot extrusion. The spray formed composites exhibit the best nano particle distribution and toughness, but the volume fraction of the nano particles that can be inserted is limited. The nano composites fabricated through the powder metallurgy method possess the highest strength due to the extra strengthening effect from the MgO phase. Strengthening analysis based on the Orowan strengthening mechanism can predict well the composite strength provided that the nano particles are in reasonably uniform dispersion. For composites containing higher nano particle volume fractions greater than 3%, the experimental strength data fall well below the theoretical predictions, suggesting poor dispersion of the reinforcement.
[doi:10.2320/matertrans.47.1985]

(Received March 6, 2006; Accepted June 14, 2006; Published August 15, 2006)

Keywords: *Mg alloy, nano particles, composites, strengthening, toughness*

1. Introduction

The success in fabricating various nano-sized powders, wires or tubes has provided the new possibility in modifying the existing commercial materials in terms of their functional or structural characteristics. Inorganic nano oxide, nitride, refractory or highly electrically conductive metallic powders may be inserted in polymers, ceramics, metals, or semiconductors by various means. Except for few reports, the major achievements were focused on the polymer matrix modified by ceramic nano particles so as to significantly improve its mechanical or physical properties. The addition of nano powders in metallic alloys has been relatively much less addressed.[1)]

The uniform dispersion of the nano reinforcements has always been a critical and difficult task. Due to the high surface area ratio, nano powders tend to cluster together, sometimes forming micro-sized aggregates. The performance of the modified alloys would sensitively depend on the filler dispersion. Based on previous experience,[1)] secondary severe deformation processing such as rolling or extrusion might be promising routes to disperse the reinforcements. In this study, the AZ61 Mg alloys with nano-sized SiO_2 particles are prepared by spray forming (SF), ingot metallurgy (IM), and powder metallurgy (PM), followed by severe hot extrusion.

Spray forming is recently considered to be a potential tool to produce advanced materials. It applies inert gas atomization of the liquid stream into variously sized droplets which are then propelled away form the region of atomization by fast flowing atomizing gas.[2–6)] Droplets are subsequently deposited and collected by a substrate on which solidification takes place. Finally a coherent and near fully dense preform is produced. The by-product micro-sized Mg powders produced during spray forming can also be utilized for the PM route.

*Corresponding author, E-mail: jacobc@mail.nsysu.edu.tw

2. Experimental Methods

The AZ61 (Mg-5.88 mass%Al-0.74 mass%Zn) alloy, purchased from the CDN Company, Deltabc, Canada, was fabricated through semi-continuous casting. Amorphous SiO_2 powders measuring ~20 nm and irregular in shape (Fig. 1(a)), with a density of 2.65 Mg/m^3, are introduced into AZ61 Mg alloys via spray forming, ingot or powder metallurgy routes, all followed by extrusion.

Spray forming was conducted with the SiO_2 nano particles pre-mixed in the AZ61 billet. Figure 2 shows the simplified schematic illustration of the SF facility. Then the billet with nano particles was spray formed under special control. An example is inserted in Fig. 2, with the dimension of 180 mm in diameter and 280 mm in height, the weight of 11.7 kg, and the density of 93% with respect to the theoretical density (or around 7 volume percent in porosity). Short heating time before spray forming was to reduce the condensation of the nano particles during melting of the Mg alloys.

While spray forming technique appears to be a promising fabrication method, it is difficult to insert a high amount of nano particles through the spray nozzle. Excessive nano particles would condense near the nozzle and block the spraying Mg melt. It follows that the ingot metallurgy (IM) and powder metallurgy (PM) methods are applied to fabricate composites with nano fillers greater than 1% in volume fraction (1 vol%).

The IM route applied the high frequency induction melting at 700°C for a short period of time under Ar atmosphere. The Ar pressure was kept at 0.2 MPa so as to suppress the Mg evaporation. The PM route used the AZ61 Mg powders measuring around 10–200 μm prepared by spray forming, with the substrate being placed further lower so as to gather more over-sprayed AZ61 Mg powders. The powders were then screened by several meshes to render a smaller size distribution within 20–50 μm, as shown in Fig. 1(b). After a self-designed wet mixing technique, the AZ61 Mg and SiO_2 powders were hot pressed in vacuum at 430°C under a pressure of 100 MPa.

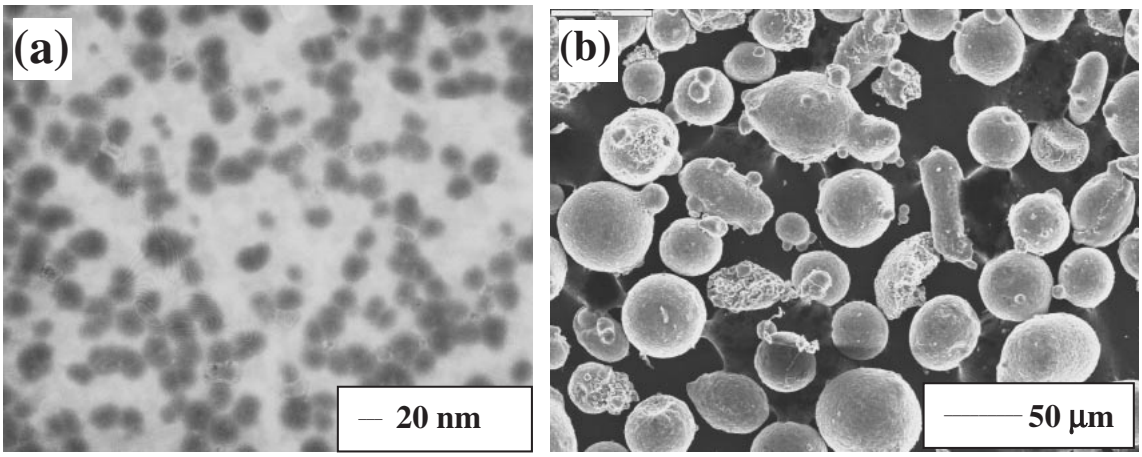

Fig. 1 (a) TEM micrograph of the nearly spherical nano SiO_2 particles, measuring ~20 nm, and (b) SEM micrograph of the nearly spherical AZ61 Mg powders prepared by spray forming, measuring ~35 μm.

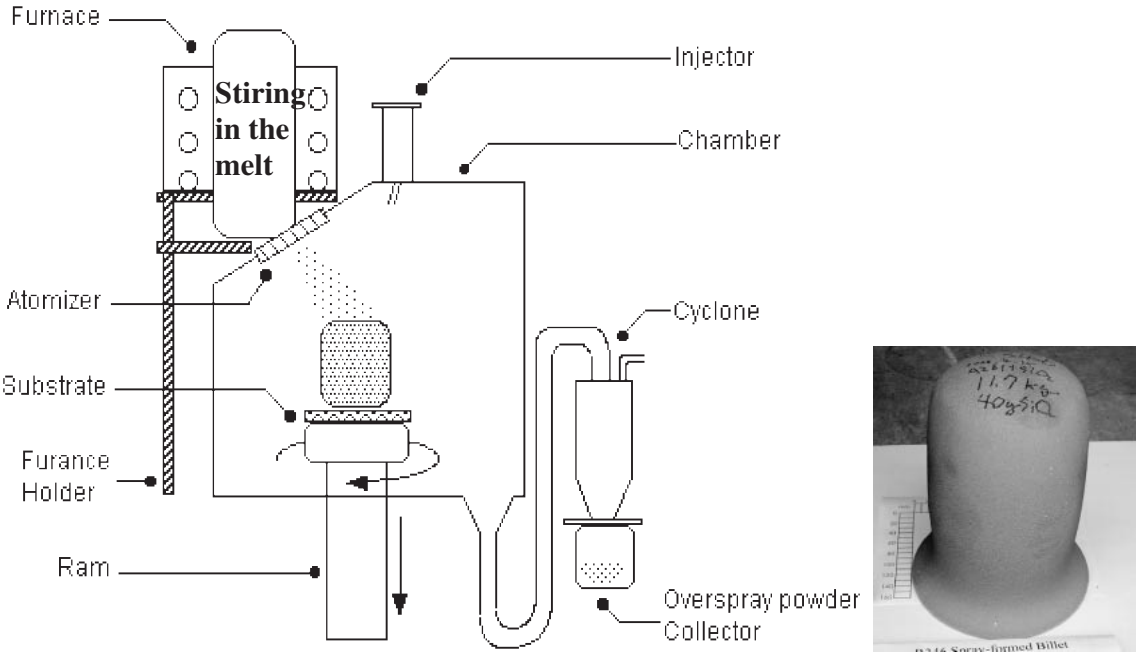

Fig. 2 Schematic illustration of the spray forming instrument and the spray formed Mg/SiO_2 composite billet, measuring 180 mm in diameter, 280 mm in length, 11.7 kg in weight, and with around 7% porosity.

Subsequent extrusion was conducted using a 350 ton hot extrutor at 300 or 400°C to an extrusion ratio of 100:1 (acting as severe deformation) to refine the microstructure and to further disperse the filler. The lower extrusion temperature of 300°C would result in more refined grain size, while the high extrusion temperature of 400°C would yield better bonding between the AZ61 Mg and SiO_2 filler. It is a trade-off dilemma depending on the user needs.

The processed specimens were then characterized by optical, scanning electron, and transmission electron microscopy (OM, SEM, and TEM), as well as Vicker's hardness measurements, tensile tests, and bending tests. The TEM thin foil specimens are prepared by ion miller. Room temperature tensile testing was conducted on the as-received billet or extruded rods along the extrusion direction, with a specimen gage length of 8.3 mm and a strain rate of 1×10^{-3} s^{-1}. The three-point bending tests were performed using an unnotched bending specimen with a specimen length of 55 mm and free span of 40 mm. The bending strain rate was calculated to be 5×10^{-4} or 1×10^{-1} s^{-1} for the low or high rate bending test, respectively.

The particle volume fraction measured from the SEM micrographs is based on the line intercept method, assuming that the 1D line fraction L_f is equal to the 2D area fraction A_f, and in turn equal to the 3D volume fraction V_f. In other words, it is assumed that particles are dispersed in a 3D random and uniform manner.

As for the measurement for TEM micrographs, the projected area fraction A'_f is transformed into the 3D volume fraction V_f using the equation[7)]

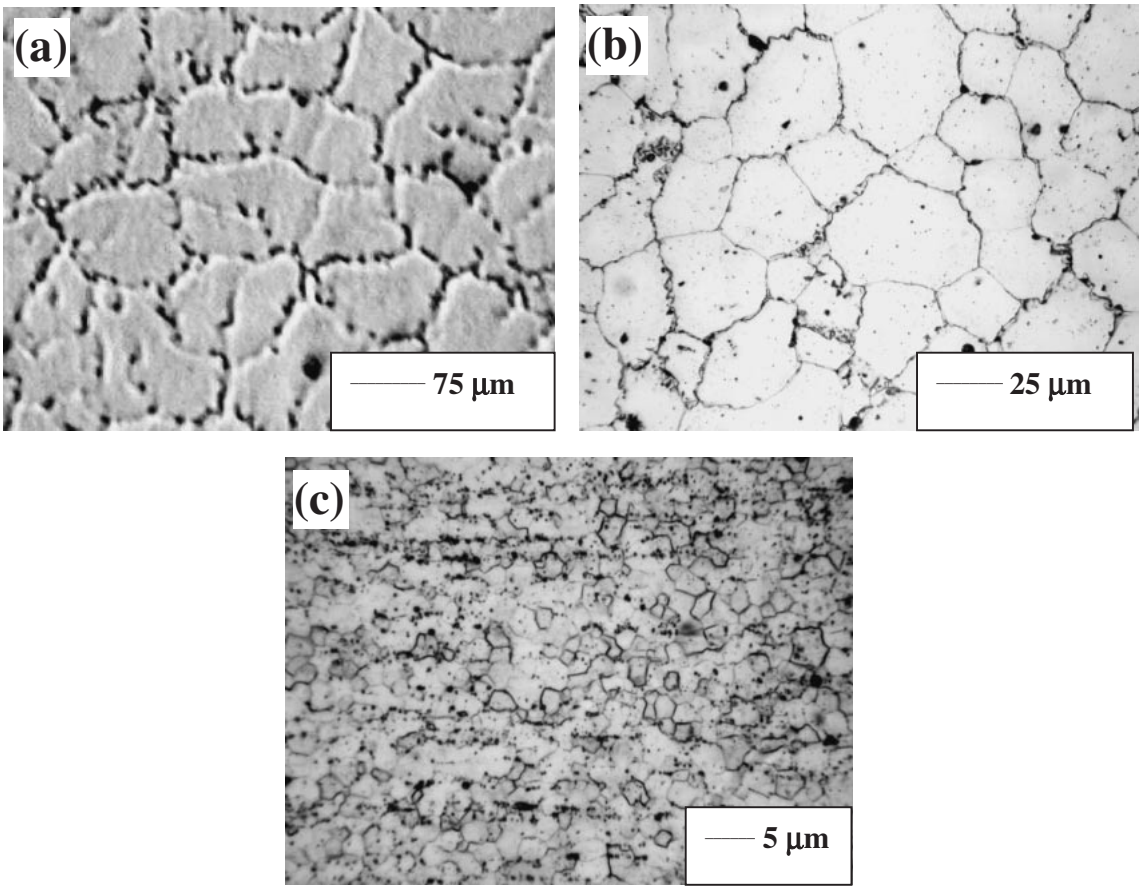

Fig. 3 The OM micrographs of (a) the as-received AZ61 billet with a mean grain size of 75 μm, (b) the as-spary-formed 0.2% composite with a mean grain size of 25 μm, and (c) the spray formed 0.2% composites after hot extrusion to 100:1 at 300°C with a mean grain size of 3.5 μm.

$$V_f = \frac{-2\langle d\rangle \ln(1 - A'_f)}{\langle d\rangle + 3t}, \quad (1)$$

where $\langle d\rangle$ is the average particle size and t the TEM thin foil thickness.

3. Results and Discussion

3.1 Microstructures

The OM micrographs of the as-received AZ61 billet and the as-SFed composite are compared in Figs. 3(a) and 3(b), showing the average grain sizes of 75 μm and 25 μm, respectively. The much refined grain size in the SFed composite is due to fast cooling and solidification rates during SF and the restriction from grain growth by the embedded tiny ceramic particles. After high ratio extrusion, the grain size was further refined to 2–10 μm, as shown an example in Fig. 3(c), dependent on the materials and extrusion temperature. Table 1 lists the resulting grain size in various materials including the SF, IM and PM specimens.

The dispersion of SiO_2 in the SF, IM and PM composites was examined under field emission SEM. There are always some dispersoids in distinct white contrast in the back-scattering electron image (BEI) micrographs, measuring around 0.2 μm in average, in both the AZ61 billet and composites, as shown in Fig. 4(a). These were identified to be the Mn bearing particles (basically Al_4Mn), with a low volume fraction around 0.05%, which should have little influence on the strengthening effect. In addition to Al_4Mn, there are a very small amount of the β ($Mg_{17}Al_{12}$) particles in the extruded composites, measuring around 1 μm. The low volume fraction of the $Mg_{17}Al_{12}$ phase in the AZ61 based SF, IM and PM composites is a result of the long thermal exposure of the composites at 300 or 400°C for 4 h before the hot extrusion. Most of the $Mg_{17}Al_{12}$ phase would be reverted into the matrix based on the Mg-Al phase diagram. The solubility of Al in Mg matrix at 300 or 400°C is around 6.5 and 10.5 mass%, greater than the 5.88 mass% Al in the

Table 1 Summary of the grain size and Hv hardness of the AZ61 composites under various material and processing conditions.

Material	Processing condition	Grain size (μm)	H_v hardness
AZ61 alloy	As-received billet	75	60
SF 0.2%SiO_2	As-spray-formed	25	56
SF 0.2%SiO_2	Extruded at 400°C	9.6	67
SF 0.2%SiO_2	Extruded at 300°C	3.5	73
IM 0.2%SiO_2	Extruded at 400°C	5.0	70
PM 0.2%SiO_2	Extruded at 400°C	6.0	74
IM 1%SiO_2	Extruded at 300°C	4.3	75
PM 1%SiO_2	Extruded at 300°C	2.8	100
IM 3%SiO_2	Extruded at 300°C	2.9	88
PM 5%SiO_2	Extruded at 300°C	3.8	102

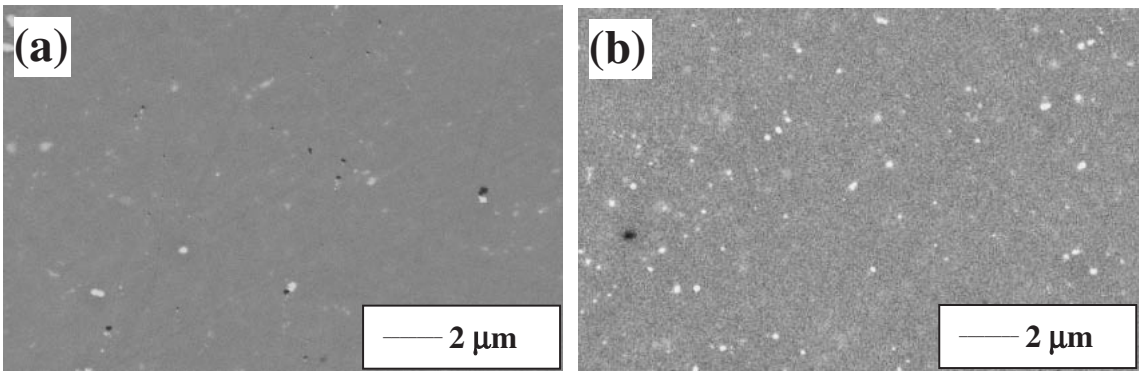

Fig. 4 SEM-BEI micrographs showing (a) the white contrast from Al_4Mn in the as-received AZ61 billet, measuring ~0.2 μm and (b) the distribution of nano SiO_2 (only the clustered regions can be resolved by SEM, appeared in faint contrast in the background and measuring ~100 nm) in the SF 0.2% composites after extrusion.

Table 2 Summary of the size and volume fraction of various particle phases present in the processed composites.

	SiO_2	MgO	Mg_2Si	Al_4Mn
SF 0.2%SiO_2	20–100 nm/~0.1%	5–10 nm/~0.08%	0.3 μm/~0.02%	0.2 μm/~0.05%
IM 0.2%SiO_2	20–1000 nm/~0.1%	5–10 nm/~0.08%	0.3 μm/~0.02%	0.2 μm/~0.05%
PM 0.2%SiO_2	20–200 nm/~0.16%	5–10 nm/~0.15%	0.3 μm/~0.01%	0.2 μm/~0.05%
IM 1%SiO_2	20–1000 nm/~0.5%	5–10 nm/~0.4%	0.3 μm/~0.1%	0.2 μm/~0.05%
PM 1%SiO_2	20–500 nm/~0.8%	5–10 nm/~0.5%	0.3 μm/~0.05%	0.2 μm/~0.05%
IM 3%SiO_2	20–1000 nm/~1.5%	5–10 nm/~1.2%	0.3 μm/~0.3%	0.2 μm/~0.05%
PM 5%SiO_2	20–500 nm/~4%	5–10 nm/~1.5%	0.3 μm/~0.08%	0.2 μm/~0.05%

current AZ61 alloy. During the relatively rapid cooling after hot extrusion for the extruded thin bars, there would also be minimum precipitation of the $Mg_{17}Al_{12}$ phase. The remaining few $Mg_{17}Al_{12}$ particles observed mostly in the IM composites (after hot extrusion) are those not fully reverted rather than further precipitated out during cooling. In what follows, the strengthening analysis does not include the contribution from $Mg_{17}Al_{12}$.

The BEI contrasts for Si and Mg are weak due to the small difference in atomic number. In the background of the SEM BEI micrographs, after image enhancement through image software, the nano particles can be traced by the faint whiter contrast, as shown in Fig. 4(b). The particles are seen to be within 20–100 nm in size in the SF composite, 20–1000 nm in the IM composites, and 20–500 nm in the PM composites, which are mostly larger than the mean size of 20 nm for the SiO_2 particles. Nano particles smaller than 20 nm are not readily resolved by the current field emission SEM.

Local clustering is still inevitable in all composites fabricated, but the distribution overall is reasonably uniform in the composites with 0.2 vol% SiO_2, prepared by SF, IM or PM followed by 100:1 hot extrusion. The 0.2% SF composite exhibited the most uniform particle distribution, while the IM composites possessed the worst dispersion due to the tendency to condensation during casting. Severe clustering of nano SiO_2 to a size up to 1 μm can be seen in the IM composites. With higher filler contents to 1–5%, clustering of the nano SiO_2 particles becomes gradually more serious. The largest filler cluster size in these composites can reach 500 nm in the PM composites and even 1000 nm in the IM ones, as listed in Table 2.

TEM characterizations have been conducted on selected composite specimens, but can only reveal the particle distribution in highly localized regions. Figure 5(a) shows an example for the 0.2% SF composite after extrusion to 100:1 at 300°C. The dark and larger particles in Fig. 5(a) are identified by EDS to be the Al_4Mn particles, measuring from 0.1–0.8 μm and with an average size of ~0.2 μm. Few needle shaped particles are the Mg_2Si phase, as a result of the phase transformation of $SiO_2 + 2Mg \rightarrow 2MgO + Si$, followed by $2Mg + Si \rightarrow Mg_2Si$. The length of Mg_2Si is typically around 0.3 μm (Table 2). In the background, there are some smaller and spherical particles in weak contrast. These are identified to be the individual or clustered amorphous SiO_2 particles. The amorphous nature of SiO_2 makes the bright field image in weak contrast. The distribution of such nano SiO_2 particles varies in different locations. But in most cases, they are in reasonably uniform dispersion, measuring from 20 to 100 nm in this SF composite (Table 2).

In contrast, the second-phase particles in the IM and PM composites, particularly with higher SiO_2 volume fractions, are seen to disperse much less homogeneously. For example, Fig. 5(b) presents a severe cluster of the nano particles measuring around 500–1000 nm in the 1% PM composite. By close examination of the enlarged TEM bright field image in Fig. 5(c), the black and strongly contrasted particles are identified to be the MgO phase, with a size for each individual fine particle of 5–10 nm. The grey and weakly contrasted particles measuring around 20–30 nm are the remaining amorphous SiO_2. The associated diffraction pattern in Fig. 5(d) shows the strong rings originated from MgO with the weak halo background around the (000) center

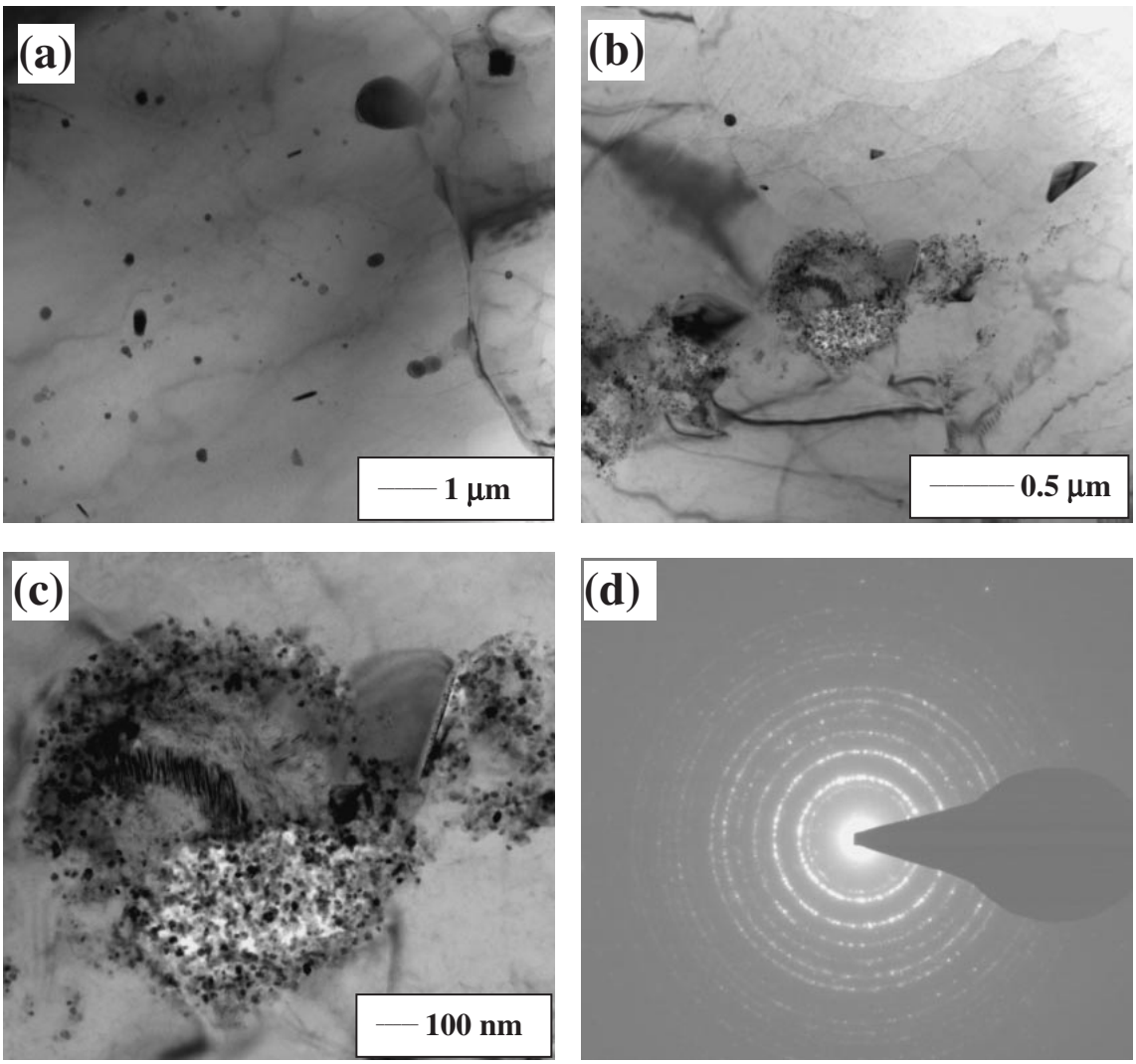

Fig. 5 TEM micrographs of the AZ61 based composites showing (a) the relatively uniform distribution of the dark and larger $A1_4Mn$, needle-shaped Mg_2Si and smaller and gray SiO_2 in the SF 0.2% composite, (b) the severe clustering of SiO_2 in the PM 1% composite, (c) the enlarged view of (b) showing the fine and black crystalline MgO (in strong contrast) mixed with the lighter amorphous SiO_2 in weak or gray contrast, and (d) the diffraction pattern taken from the clustering region in (c) showing the rings from crystalline MgO (with the weak halo intensity from the amorphous SiO_2 overshadowed by the rings patterns).

originated from the amorphous SiO_2. Overall, around 20% of the amorphous SiO_2 in volume fraction has been transformed into crystalline MgO nano particles. In the PM composites, there are extra amounts of MgO formed on the AZ61 powder surfaces during spray forming.

Based on the SEM and TEM phase analyses and quantitative measurements, there are various amounts of different phases, such as amorphous SiO_2 (~20 nm in size and 100–1000 nm in cluster size), MgO (~5–10 nm), Mg_2Si (~0.3 μm), and Al_4Mn (~0.2 μm) in the processed composites. Due to the different working temperatures applied during the SF, IM and PM processes, the resulting sizes and volume fractions of such phases in these composites also vary accordingly. Table 2 summarizes the average measured values.

3.2 Mechancal properties

The hardness and tensile results are summarized in Tables 1 and 3, respectively. The H_v Vicker's hardness,

Table 3 Summary of the room temperature tensile properties of the AZ61 alloy and composites under various material and processing conditions.

Material	Processing condition	YS (MPa)	UTS (MPa)	Elongation
AZ61 alloy	As-received billet	112	181	15%
SF 0.2%SiO_2	As-spray-formed	—*	—	—
SF 0.2%SiO_2	Extruded at 400°C	247	316	35%
SF 0.2%SiO_2	Extruded at 300°C	263	340	32%
IM 0.2%SiO_2	Extruded at 400°C	280	345	18%
PM 0.2%SiO_2	Extruded at 400°C	268	351	27%
IM 1%SiO_2	Extruded at 300°C	230	290	18%
PM 1%SiO_2	Extruded at 300°C	330	379	7%
IM 3%SiO_2	Extruded at 300°C	234	310	15%
PM 5%SiO_2	Extruded at 300°C	281	284	4%

*Data are subject to great uncertainty due to the presence of 7% porosity under this condition

Table 4 Summary of theoretical predictions for each second phase particles (SiO_2, MgO, Mg_2Si, Al_4Mn) and the overall CRSS τ_o based on the (1) linear addition rule, τ_{o1}, and (2) Pythagorean (or squre) addition rule, τ_{o2}.

Material	Processing condition	τ_{SiO_2} (MPa)	τ_{MgO} (MPa)	τ_{Mg_2Si} (MPa)	τ_{Al_4Mn} (MPa)	τ_{o1} (MPa)	τ_{o2} (MPa)
AZ61 alloy	As-received billet	0	0	0	0.88	0.88	0.88
SF 0.2%SiO_2	As-spray-formed	6.56	11.32	0.39	0.88	19.15	13.12
SF 0.2%SiO_2	Extruded at 400°C	6.56	11.32	0.39	0.88	19.15	13.12
SF 0.2%SiO_2	Extruded at 300°C	6.56	11.32	0.39	0.88	19.15	13.12
IM 0.2%SiO_2	Extruded at 400°C	6.56	11.32	0.39	0.88	19.15	13.12
PM 0.2%SiO_2	Extruded at 400°C	8.38	15.65	0.28	0.88	25.19	17.78
IM 1%SiO_2	Extruded at 300°C	15.32	26.23	0.28	0.88	42.71	30.39
PM 1%SiO_2	Extruded at 300°C	19.83	29.69	0.63	0.88	51.03	35.72
IM 3%SiO_2	Extruded at 300°C	28.38	48.09	1.59	0.88	78.94	55.87
PM 5%SiO_2	Extruded at 300°C	51.60	55.16	0.79	0.88	108.43	75.54

yield stress (YS), and ultimate tensile stress (UTS) data on the processed composites all show different levels of strengthening with the addition of nano reinforcements, as compared with the as-received AZ61 billet. The strengthening is a result of both grain refinement and dispersion hardening, as analyzed in the next section. The PM composite with 1 vol% SiO_2 possesses the highest YS (330 MPa) and UTS (379 MPa), due to the additional MgO oxides formed on the surface of AZ61 Mg powders during spray forming. However, with higher SiO_2 fillers to 3 and 5 vol%, even with continuous increment in hardness, the tensile YS and UTS start to decline appreciably as a result of more severe filler clustering.

The tensile elongation of the SF composites (over 30%) is higher than those of the AZ61 billet and all composites made by other routes, suggesting more uniform particle distribution. In contrast, the PM composites with 1 and 5 vol% SiO_2 tend to exhibit low elongations of 4–7%, presumably also due to the ill bonding of the Mg powders which usually contain thin MgO layers on the powder surface formed during spray forming.

3.3 Strengthening analyses

The strengthening effects of the nano composites are characterized by the Orowan equation, since the second phases (SiO_2, MgO, Mg_2Si, and Al_4Mn) found under TEM are either ceramics in nature or large in size, thus are all non-shearable be dislocations. Strong dislocation bowing and tangling around the particles have been seen under TEM. The strengthening analysis resembles those used for dispersion hardening alloys. The critical resolved shear stress (CRSS) τ can be expressed as[8)]

$$\tau = 0.81 \frac{Gb}{2\pi(1-\nu)^{1/2}(L_s - 2r_s)} \ln\left(\frac{2r_s}{b}\right), \qquad (2)$$

where G is the shear modulus, $\boldsymbol{b}$ the Burger's vector, ν the Poisson ratio, L_s the mean distance between reinforcements, and r_s the radius of reinforcements. The dislocation line tension integral is taken as $\ln(2r_s/b)$ here due to the dislocation utter cut-off distance would be very small for highly curved dislocations during the Orowan bowing process. The mean interparticles spacing L_s can be assessed via the equation[9)]

$$L_s = r\sqrt{\frac{2\pi}{3V_f}}, \qquad (3)$$

where V_f is the volume fraction of the second phase.

Using the data for Mg, namely, $G = 17$ GPa, $\nu = 0.35$, and $\boldsymbol{b} = (1/3)[2\bar{1}\bar{1}0]$ for the active Burger's vector at room temperature, the theoretical CRSS values calculated on the base of the Orowan strengthening from eq. (1) for the four major second phases are listed in Table 4. Due to the very small amount and very large in size for the Mg_2Si and Al_4Mn phases, the CRSS values for these two particles are considerably smaller, typically less than 1 MPa. Thus the major Orowan strengthening came from the nano SiO_2 and MgO phases, the CRSS varies from 6 to 55 MPa for various composites.

There have been numerous propositions for the addition rules suitable for adding the individual strengthening contributions.[10–12)] The most common ones are the linear and Pythagorean (or square) addition rules, namely,

$$\tau_o = \tau_1 + \tau_2, \qquad (4)$$

and

$$\tau_o{}^2 = \tau_1{}^2 + \tau_2{}^2. \qquad (5)$$

For all of the four second-phase particles observed in the current composites, they are strong obstacles forcing the dislocations to bow around the particles. The suitable superposition rule to add up such equal strength obstacles should be the Pythagorean (or square) addition rule.[9)] Table 4 includes the overall CRSS contributed by these four obstacles based on the linear (t_{o1}) and Pythagorean (t_{o2}) addition rules. Previous rigorous studies have tried the addition rule with an adjustable exponent q, or $\tau_o{}^q = \tau_1{}^q + \tau_2{}^q$,[9,13,14)] and $q = 1$ and 2 would yield eqs. (3) and (4), respectively. Since the force profiles for obstacles 1 and 2 would not be exactly in phase, thereby the linear addition rule to simply add up the two contributions from both obstacles tends to overestimate the actual situation. It follows that τ_{o2} is in use for the subsequent analysis for the composite strengthening.

Moreover, it is known that the YS of a polycrystalline specimen can be transferred from the CRSS by multiplying the Taylor factor, M, i.e., YS $= \tau \times$ M. The Taylor factor M is related to the texture of the material and is often in the range of 2–4.[15)] For the current fully recrystallized and fine-

Table 5 The theoretical strengthening values using the pythagorean (or square) addition rule compared with the experimental data obtained by tensile tests.

Material	Processing condition	Orowan σ_o ($\tau_o \times 3$) (MPa)	Hall-Petch σ_{HP} (MPa)	Theo YS σ_{theo} (MPa)	Exp YS σ_{exp} (MPa)
AZ61 alloy	As-received billet	3	96	99	112
SF 0.2%SiO_2	As-spray-formed	39	126	165	—
SF 0.2%SiO_2	Extruded at 400°C	39	168	207	247
SF 0.2%SiO_2	Extruded at 300°C	39	242	281	263
IM 0.2%SiO_2	Extruded at 400°C	39	211	250	280
PM 0.2%SiO_2	Extruded at 400°C	53	198	251	268
IM 1%SiO_2	Extruded at 300°C	91	225	316	230
PM 1%SiO_2	Extruded at 300°C	107	264	371	330
IM 3%SiO_2	Extruded at 300°C	168	260	428	234
PM 5%SiO_2	Extruded at 300°C	227	235	462	281

grained AZ61 alloys or composites after hot extrusion, the texture intensity was seen to be weak[16] so that M is taken to be around 3. The first row in Table 5 lists the predicted YS values attributed by the Orowan strengthening, i.e., $\sigma_o = \tau_{o2} \times 3$.

In addition to the Orowan strengthening contribution, the fine grain size strengthening should also be considered. The Hall-Petch relationship for the AZ-series Mg alloys has been established, based on massive experimental data, as $\sigma_{ys} = 56 + 348d^{-1/2}$ (in units of MPa and μm, respectively).[16] The calculated grain size strengthening values, σ_{HP}, for various composites possessing different grain sizes are also listed in Table 5.

The linear superposition rule for the overall Orowan and grain size strengthening contributions is universally applied. Table 5 compiles the theoretically calculated YS, σ_{theo}, by linearly adding the σ_o and σ_{HP}, ranging from 99 MPa for the as-received AZ61 billet to 462 MPa for the PM 5% composites. These theoretical values can be compared with the experimentally measured YS, σ_{exp}, as listed in the last column of Table 5. It can be seen that for the AZ61 billet and the composites containing lower nano particle contents, the agreement between σ_{theo} and σ_{exp} is reasonably good. However, for higher filler contents, especially for the 3% and 5% composites, the experimental data are significantly lower than the theoretical predictions. The comparison can be more readily seen from the plot in Fig. 6. The largest discrepancy occurs for the IM 3% and PM 5% composites, where σ_{exp} is lower than σ_{theo} by 194 and 181 MPa, respectively. The experimental observed yield strengths for these latter specimens are largely contributed by the grain size strengthening. The inclusion of 3–5 vol% nano particles into the AZ61 alloy did not lead to the effective hardening, obviously a result of more severe particle clustering.

Since the Hall-Petch relationship is most likely to be obeyed in the AZ61 alloy and composites, it is meaningful to plot the experimental data on YS obtained from the AZ61 as-received billet, the SF, IM and PM composites against the $d^{-1/2}$, as shown in Fig. 7(a). Although most of the composite yield stresses are above the theoretical prediction based on the AZ61 alloy matrix, there are still few data fall close or even lower than the predicted Hall-Petch line. The strengthening contribution from the nano second phases in various

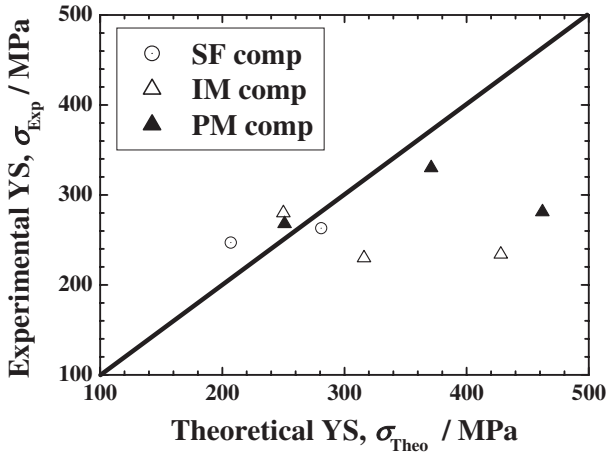

Fig. 6 The comparison of the experimentally measured yield stress and the theoretically predicted yield stress for the various composites fabricated.

composites can be more readily seen from the net stress increment excluding the Hall-Petch contribution. This is done by linearly extracting the σ_{HP} from the experimental data σ_{exp}, and by plotting ($\sigma_{exp} - \sigma_{HP}$) against the SiO_2 volume fraction, as presented in Fig. 7(b). This plot would reflect the net contribution from nano SiO_2 and other resulting second phases as a function of the inserted SiO_2 volume fraction. From Fig. 7(b), it can be seen that for the 0.2 and 1 vol% specimens, the experimental data lie mostly close to or even above the theoretical prediction (the fitted solid line). However, the cases for the 3 and 5 vol% are reversed. This means that the Orowan strengthening in the 3 and 5 vol% composites are not fully revealed, due to most likely the local clustering of nano SiO_2 particles.

In past, the metal matrix composites usually insert 15–25 vol% micro-sized (1–20 μm) particulate reinforcements. The particle distribution with or without secondary rolling or extrusion are mostly satisfactory. However, the composites reinforced by the nano particles (5–30 nm) are subject to serious clustering problem when the volume fraction exceeding 3%. This ease in condensation of the nano particles during melting, coupled with the difficulty in flowing into uniform dispersion during solid-state plastic deformation, both lead to the cluster defect. For polymer matrix nano

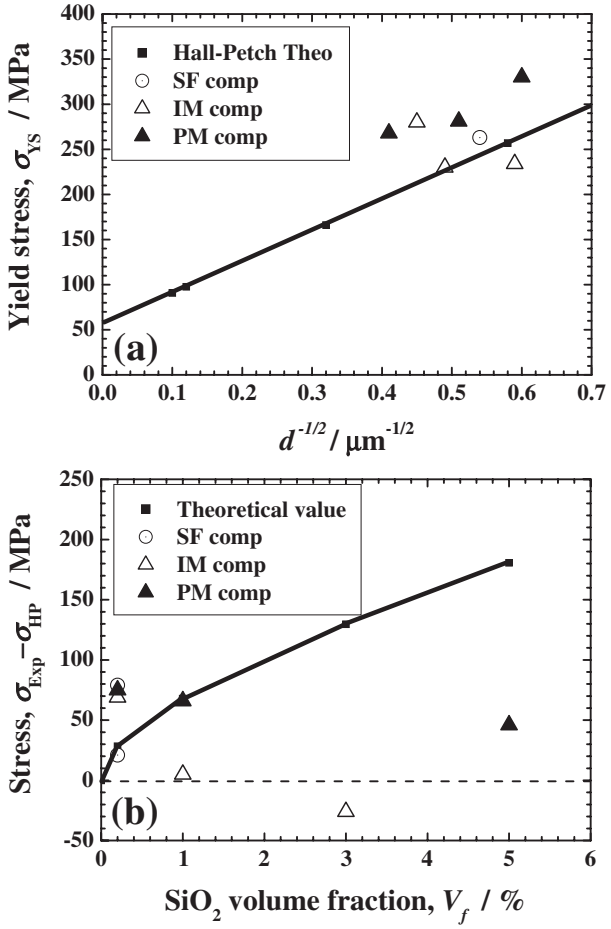

Fig. 7 (a) The Hall-Petch plot for the experimentally measured yield stress of the fabricated composites, and (b) the net contribution from the nano second phases to the experimentally measured yield stress, with the Hall-Petch grain size strengthening excluded, i.e., $\sigma_{Exp} - \sigma_{HP}$, as a function of the inserted SiO_2 particle volume fraction.

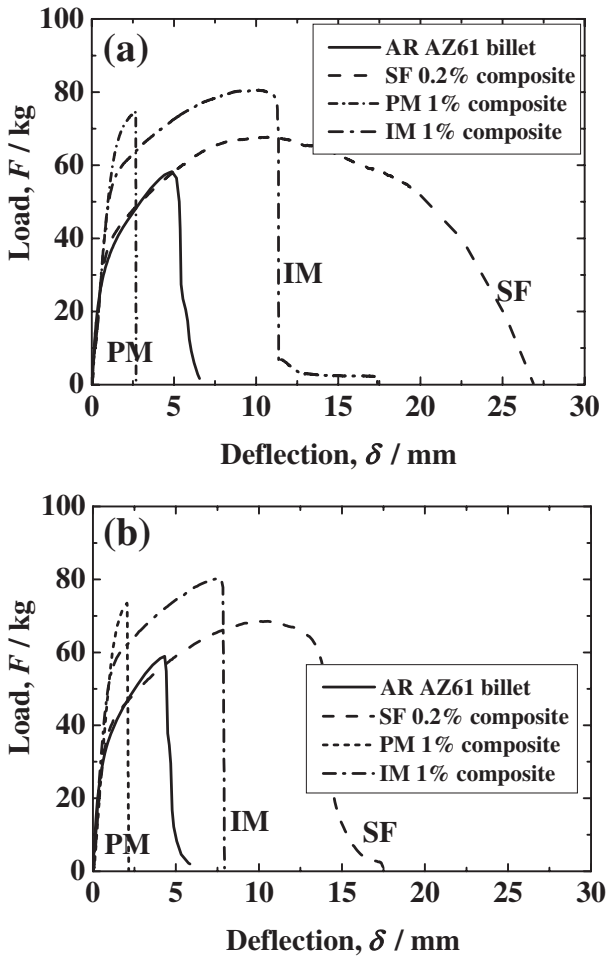

Fig. 8 The bending load-deflection plots of the AZ61 billet and composites at (a) low strain rate ($5 \times 10^{-4}\ s^{-1}$) and (b) high strain rate ($1 \times 10^{-1}\ s^{-1}$).

composites, the filler content can be added up to 10 vol%,[17] taking advantage of the viscous flow behavior above the glass transition temperature. Without such a characteristic in metals, it seems that a more rigorous plastic flow is needed. The current extrusion to an extrusion ratio of 100:1 did not seem to be sufficient. Other severe plastic deformation means such as equal channel angular extrusion or friction stir processing might be feasible. Recent trial of the same AZ61/SiO_2 composites prepared by four-pass friction stir processing has demonstrated the more promising results.[18]

3.4 Toughness

The toughness of the composites was investigated via the bending tests. Both the low strain rate ($5 \times 10^{-4}\ s^{-1}$) and high strain rate ($1 \times 10^{-1}\ s^{-1}$) loadings were employed. Figure 8 shows the typical load-deflection curves of the AZ61 billet and composites. It can be easily seen that the toughness is much higher at low rates. For most cases, the loads of the bending specimens fall rapidly after peak load, suggesting the weak resistance against existing cracks. The SF composite reveals the opposite behavior, where the specimen can sustain continuous deflection after peak load to nearly 20 mm.

Table 6 lists the bending results in terms of the peak load (F_p), deflection to peak load (δ_p), total deflection (δ_t), crack initiation energy (E_i, or the integrated energy before the peak load), crack propagation energy (E_p, or the integrated energy after the peak load), total energy (E_t), as well as the ductility index (DI), which is defied as E_p/E_i. If the specimen exhibits relatively higher propagation energy after crack formation,

Table 6 The toughness obtained via triple point bending tests on specimens extruded at 300°C.

	F_p (kg)	δ_p (mm)	δ_t (mm)	E_i (J)	E_p (J)	E_t (J)	DI
Low rate ($5 \times 10^{-4}\ s^{-1}$)							
AR AZ61 billet	58	4.80	6.67	2.08	0.27	2.35	0.130
SF 0.2%	67	9.80	26.87	4.89	8.56	13.45	1.751
IM 1%	80	10.17	17.38	6.23	1.41	7.64	0.226
PM 1%	74	2.65	2.69	1.33	0.02	1.35	0.015
IM 3%	53	8.70	15.29	3.49	0.60	4.09	0.172
PM 5%	60	2.37	2.42	0.97	0.01	0.98	0.010
High rate ($1 \times 10^{-1}\ s^{-1}$)							
AR AZ61 billet	58	4.30	5.85	1.87	0.23	2.10	0.123
SF 0.2%	68	10.00	17.5	5.40	2.80	8.30	0.519
IM 1%	80	6.84	7.92	4.84	0.18	5.02	0.037
PM 1%	73	2.07	2.16	0.89	0.03	0.92	0.033

the material resistance to catastrophic failure is higher, and the toughness or ductility of the material, or the DI, is considered to be higher.

The SF composites exhibit reasonably high peak δ_p, δ_t, E_i, E_p, E_t and DI, consistently with the higher tensile elongation as presented in Table 3. The higher tensile elongation and bending properties directly indicate the higher toughness and indirectly imply the relatively more uniform dispersion of the nano particles. In contrast, the 1 and 5 vol% PM specimens always exhibit much lower deflections (δ_p and δ_t both less than 3 mm), as well as low E_t ($\sim$1 J) and low DI (0.01–0.03). The IM composites fall in-between the SF and PM counterparts.

In comparing Figs. 8(a) and 8(b), which represents the low rate and high rate bending tests, composite specimens subjected to low rate bending exhibited higher deflections, while the maximum loads are almost the same. When the samples are bent at low rates, they tend to undergo a certain level of plasticity before and after microcrack initiation (occurring near the peak load stage). While bent at high rates, cracks would propagate rapidly and plastic deformation did not seem to catch in time. It is worth noting that the SF samples can sustain higher deflections both at low and high rates, suggesting the better toughness under different loading conditions.

For practical application, the DI index is preferred to be greater than 1.0, thus the SF composite perform better in this aspect. The spray forming technique is demonstrated to offer an effective route to prepare composites with nano reinforcements. Further improvement to control the spray forming process is worth trying. Separate spraying of the Mg melt and nano particles through two separate nozzles might lead to better particle distributions and higher amounts of nano particles to be sprayed.

4. Summary

The AZ61 Mg based composites containing SiO_2 particles measuring 20 nm in diameter were prepared either by spray forming, ingot metallurgy, or powder metallurgy, followed by severe hot extrusion to 100:1 at 300–400°C. The grain size of the resulting composites is around 2–4 μm as extruded at 300°C and around 5–10 μm as extruded at 400°C. Some of the amorphous SiO_2 nano particles would transform into MgO measuring 5–10 nm and Mg_2Si measuring around 0.3 μm. In addition, there are small amounts of Al_4Mn particles measuring around 0.2 μm formed in the AZ61 billet as well as in all composites fabricated.

In comparison, the spray formed composites exhibit the best nano particle distribution and tensile elongation, but the volume fraction of the nano particles that can be inserted is limited. The nano composites fabricated through the powder metallurgy method posses the highest strength due to the extra strengthening effect from the MgO phase. Strengthening analysis based on the Orowan strengthening mechanism for the SiO_2, MgO, Mg_2Si and Al_4Mn phases can predict well the composite strength provided the nano particles are in reasonably uniform dispersion. For composites containing higher nano particle volume fraction to 3% or above, the experimental strength data fall well below the theoretical predictions.

The toughness of the AZ61 billet and the fabricated composites are evaluated by the three-point bending at low and high rates. The SF composite again exhibits the highest deflection, fracture energy, and ductility index, consistent with the tensile elongation. The PM composites fail at a considerably low toughness, presumably due to the ill bonding of the Mg powders which usually contain thin MgO layers on the powder surface formed during spray forming.

Acknowledgements

The authors gratefully acknowledge the sponsorship by National Science Council of Taiwan, ROC, under the projects NSC 92-2216-E-110-017 and NSC 92-2216-E-006-037.

REFERENCES

1) T. D. Wang and J. C. Huang: Mater. Trans. **42** (2001) 1781–1789.
2) A. R. E. Siger: Met. Mater. **4** (1970) 246–252.
3) B. Williams: Met. Powder Rep. **35** (1980) 464–470.
4) S. Spangel, E. Matthaeischulz, A. Schulz, H. Vetters and P. Mayr: Mater. Sci. Eng. **A326** (2002) 26–39.
5) C. Y. Chen and ChiY. A. Tsao: Mater. Sci. Eng. **A383** (2004) 21–29.
6) Y. H. Frank Su, Y. C. Chen and ChiY. A. Tsao: Mater. Sci. Eng. **A364** (2004) 296–306.
7) E. E. Underwood: *Quantitative Stereology*, (Addition Wesley, Reading, New York, 1970) 173–178.
8) P. M. Kelly: Scripta. Metall. **6** (1972) 647–656.
9) A. J. Ardell: Metall. Trans. **16A** (1985) 2131–2165.
10) L. M. Brown and R. K. Ham: *Strengthening Methods in Crystals*, (Halsted Press Division, John Wiley & Sons, New York, 1970) 9–15.
11) R. Labusch: Phys. Stat. Sol. **41** (1970) 659–666.
12) G. Neite, M. Sieve, M. Mrotzek and E. Nebach: *Proc. 4th Risϕ Int. Syposium on Metallurgy and Materials Science*, (Risϕ National Lab., Roskilde, Denmark, 1983) 447–453.
13) J. C. Huang and A. J. Ardell: Acta Metall. **36** (1988) 2995–3006.
14) A. W. Zhu, A. Csontos and E. A. Starte, Jr.: Acta Mater. **47** (1999) 1713–1721.
15) G. I. Taylor: J. Inst. Metals **62** (1938) 307–313.
16) H. K. Lin and J. C. Huang: Mater. Trans. **43** (2002) 2424–2432.
17) M. C. Kuo and J. C. Huang: Mater. Chem. Phys. **90** (2005) 185–195.
18) C. J. Lee, J. C. Huang and P. J. Hsieh: Scripta Mater. **54** (2006) 1415–1420.